Originally published as:

Walter, T. R., Ratdomopurbo, A., Subandriyo, Nurnaning, A., Brotopuspito, K., Salzer, J. T., Lühr, B.-G. (2013): Dome growth and coulée spreading controlled by surface morphology, as determined by pixel offsets in photographs of the 2006 Merapi eruption. - *Journal of Volcanology and Geothermal Research*, *261*, 121-129.

DOI:10.1016/j.jvolgeores.2013.02.004.

Dome growth and coulée spreading controlled by surface morphology, as determined by pixel offsets in photographs of the 2006 Merapi eruption

Thomas R. Walter (1*), Antonius Ratdomopurbo (3), Subandriyo (2), Nurnaning Aisyah (2), Kirbani Sri Brotopusptio (4), Jacqueline Salzer (1), Birger Lühr (1)

(1) Dept. Physics of Earth, GFZ German Research Centre for Geosciences, Telegrafenberg, 14473 Potsdam, Germany
(2) Volcano Technical Research Center (BPPTK), Jalan Cendana 15, Yogyakarta 55166, Indonesia
(3) Earth Observatory of Singapore, Nanyang Technological University, 50 Nanyang Avenue, Singapore 639798
(4) Laboratory of Geophysics, Department of Physics, Faculty of Mathematics and Natural Science, Universitas Gadjah Mada (UGM), Yogyakarta, Indonesia

* Corresponding author: Thomas R. Walter; Email: twalter@gfz-potsdam.de; ph: +49 (0)331 288 1253; fax: +49 (0)331 288 1204

ABSTRACT. At many explosive volcanoes viscous domes extrude, which are destroyed by complete or partial collapses of the domes and the associated talus region. Although the growth and development of silicic domes and the associated flow and collapse mechanisms are of vital importance for understanding the occurrence and scale of pyroclastic flows, quantitative measurements of dome deformations are limited. We report on a sequence of photographs taken of a growing and deforming dome. A sequence in 2006 featuring the Merapi dome taken from similar camera positions allows the application of a digital image correlation algorithm, the aim being to detect and explore the temporal evolution of pixel offsets. The results suggest that the dome underwent deformation in two regions between September and October 2006: (i) dome growth and spreading at the volcano summit and (ii) coulée flow through a narrow canyon. The latter is associated with strain localization and flow acceleration, which indicates that the displacements and flow velocities at silicic domes are governed by the topographic structure into which the flows develop. The downslope motion of the distal parts of the flow and apron slumps continued during episodes of dome extrusion by gravitational spreading. An analysis of the 2006 Merapi dome and coulée displacement also provides insights into processes of the newly established southerly eruption direction, which also controlled the 2010 eruption.

Keywords: Merapi volcano, silicic dome growth, camera imaging, deformation monitoring

1. INTRODUCTION

Viscous lava domes have extruded from the Merapi volcano in Indonesia (figure 1) since before the written record (Hartmann, 1934; Hartmann, 1935). Recent dome destruction and eruption events have occurred at intervals of 4 to 6 years. The recurrent and hazardous form of dome extrusion at the Merapi volcano has received special attention (Voight et al., 2000a; Voight et al., 2000b). Merapi lava domes are commonly highly silicic and gas enriched. The emplacement of the domes in the irregularly shaped summit region and the formation of oversteepened lava dome slopes lead to destructive mass wasting events, including explosive fragmentation and the formation of block and ash (pyroclastic) flows (Abdurachman et al., 2000). Collapse events at dome-building volcanoes can be triggered by endogenous (internal) forcings associated with magmatic pressurization (Watts et al., 2002). Collapse events at Merapi have been related to extrinsic changes, such as heavy rainfall and earthquake triggering (Carn et al., 2004; Voight et al., 2000a; Walter et al., 2007). These collapse events result in the partial or total mobilization of the previously emplaced dome, and possibly lead to the unloading of the volcano and a renewed phase of magmatism (Voight et al., 2000b).

Because of the complexity of these interconnected processes, the detailed mechanisms of destabilization prior to the collapse of a dome are only partially understood. Recent accounts describe domes as complexes consisting of a lava dome core, a talus region and pyroclastic flow deposits (Wadge et al., 2008). Observations from well-monitored dome-building volcanoes, such as in Montserrat, suggest that the talus of a dome is a particularly important factor in the stability of the dome and can lead to dome destabilization if removed (Voight and Elsworth, 2000). At Montserrat, erosion of the talus by heavy rainfall initiated a sequence of collapses that removed 95% of the dome by March 2000 (Calder et al., 2002; Carn et al., 2004). Other collapse events at Montserrat also initiated at the dome talus and incised backward into the dome’s core (e.g., in July 2003; Carn et al., 2004). The above described Montserrat event highlight the importance of the talus region for the stability of a silicic dome, similarly as other occurrences did at, e.g., Mount Unzen (Japan) and Santiagito (Guatemala) (Carn et al., 2004).

Theoretical studies also suggest that dome instability and internal deformation commences long before the dome’s gravitational collapse (Hale et al., 2009a; Hale et al., 2009b; Zavada et al., 2009). Analysis of some dome collapses has revealed that the talus is a critical component for the stability of potentially explosive domes such as those at Merapi (Voight and Elsworth, 2000). The domes at the Merapi volcano have developed into an elongate talus region and have often transformed into a coulée, which is a morphologic phase between conventional lava flows and domes (Fink and Anderson, 2000). In other words, the talus region, which typically consists of debris from the dome, may physically behave as a flow. The displacement rate of a coulee can always suddenly increase and/or collapse to form block and ash flows (Voight et al., 2000a).

Year-round monitoring has taken place at the Merapi volcano since the 20th century. The monitoring is organized by the Merapi Volcano Observatory, now BPPTK, which is a branch of CVGHM, and many international partners from the USA, France, Germany, Italy, Japan and other countries. These observations have yielded detailed studies of seismology (Ratdomopurbo and Poupinet, 2000) and deformation (Young et al., 2000) of the volcano and concise summaries of recent eruptions (Surono et al., 2012).

Prior to eruptions, periods of inflation affecting the wider volcano flanks generally correspond to lava dome growth, whereas periods of deflation follow lava dome destruction and pyroclastic flow formation. Since ~20 years, in situ deformation measurements, mainly from GPS and EDM networks, have been acquired continuously on the lower flanks of the volcano and in campaign mode in the near-dome region

(Jousset et al., 2000; Young et al., 2000). Direct quantification of the volume changes of the domes remains difficult. The processes of dome growth, its internal deformation and exogenous versus endogenous morphology changes also remain to be studied. Assessing dome growth accompanied by explosions was previously limited to visual observations (Ratdomopurbo, 1995; Ratdomopurbo et al., this volume).

The present paper focuses on the morphologic changes and movement of a coulée and the difference in growth at the upper dome and in the coulée region. Dome-building activity at the Merapi volcano was recorded by digital photography in September and October 2006 and was analyzed using modern image correlation methods to quantify the systematic offsets of pixels and deformation of the silicic dome. The results suggest that the emplaced domes deform vertically and laterally and that gravitational spreading plays a role in the deformation. The dome growth described includes detectable coulée displacement that is most pronounced in a narrow valley through which the rock mass flows. This finding leads us to propose a dome flow mechanism in a bottleneck that laterally constrains the rock mass and affects its strain and flow velocity.

2. METHODS

Images capturing the 2006 eruption were taken at irregular sampling intervals from a variety of positions that were mainly located at or near the volcano observatory posts (from where the volcano is monitored continuously), such as at Ngepos (11 km to the southwest of the summit), Plawangan (5 km to the west) and Kaliurang (7 km to the south of the volcano). Such time-lapse photography are of high value for the daily operation of the volcano observatory (Ratdomopurbo et al., this volume). For this study, we utilized images taken near the village of Deles (7.566° S, 110.464° E; see figure 2), approximately 4 km south-southeast of the summit of Merapi. After the main eruption that peaked on 9 and 14 June 2006, dome and crater rim collapse events formed a new and extensive incision to the south into the Gendol Valley (Charbonnier and Gertisser, 2009); the incision is shown in late-2006 satellite imagery (figure 2). The valley also directed most of the pyroclastic flows southward during the 2010 eruption, which led to multiple fatalities (Surono et al., 2012).

The images analyzed in this study were taken with digital SLR cameras, such as a Canon EOS 350D DIGITAL (18 Sept – 29 Sept 2006) at 3456x2304-pixel resolution and a NIKON D70s (13 Oct – 30 Oct 2006) at 3008x2000-pixel resolution. The photos were taken consistently with a 200 mm focal length, which, in combination with the similar APS-C sensor of the two cameras, provided similar fields of views. To correct for the use of different cameras and enhance the quality of the images, we initially stacked the photos by applying a shift and rotation procedure common in image-stitching and matching approaches. The application of this algorithm resulted in a field of view of approximately 490 m in the x-axis at the summit distance, which translates to pixel dimensions of 0.14 m and 0.16 m resolution for the two cameras, respectively. We then resampled the images at a similar resolution to obtain a pixel dimension of approximately 1x1 m^2. This image dimension was also chosen to ease the transformation from the pixel to the meter scale and to reduce other image noise, such as that arising from image compression. It should be noted that we did not correct for more complex geometric distortion effects, which is why the 1x1 m^2 pixel dimension is only approximate. Because the images were taken at different times of day, the illumination directions and white balances were irregular; we attempted to correct this problem by image-intensity normalization. After these image-preprocessing steps, we could use nine images that were taken between 18 and 29 Sept 2006 (figure 3).

To analyze the pixel offsets, we considered each of the images as a two-dimensional intensity matrix. A pixel was defined at a coordinate $U = (x, y)$ in the first image, which is referred to as the reference image. Utilizing a second image, a signal was represented as a shifted copy of the former reference image (Pan et al., 2009) so that the image intensity function is defined by

$$I(x,y,t) = I(x+u, y+v, t+\Delta t) \quad (1)$$

, where (u, v) is the displacement after a time increment Δt. These simple transformations were used to shift the image globally and match it with the other images, as described previously. We then adaptively divided the image into pre-defined subregions to increase the spatial resolution and accuracy of the pixel-offset detection technique (Adrian, 1991). The subregion dimensions were defined arbitrarily at first but were later selected based on the expected deformation being less than 50% of the first pass. The subregions that we defined have initial $n \times m$ dimensions of $32 \times 32\,pixels$ and overlap by 75%; these parameters decrease in the second pass to $16 \times 16\,pixels$ and 50% overlap. An example of the subregions and their lateral shift is illustrated in figure 4. We also tested subregions with different sizes but found this configuration to be the most robust for the selected database. By solving the squared Euclidean distance between the two subregions in the first image I_M and the second image I_S, we obtain

$$d^2(u,v) = \sum_{x=-n}^{n} \sum_{y=-n}^{n} [I_M(x,y) - I_S(x+u, y+v)\,]^2, \quad (2)$$

which is intended to pair each pixel with a corresponding pixel. Because this general formulation assumes an image intensity, given by

$$\sum I_S^2(x+u, y+v), \quad (3)$$

which is nearly constant, the cross-correlation term may be reformulated to test the similarities between the pre-defined subregions according to the following:

$$c^2(u,v) = \sum_{x=-n}^{n} \sum_{y=-n}^{n} I_M(x,y) - I_S(x+u, y+v). \quad (4)$$

Although this approach has strengths, some limitations exist. Natural photographs are commonly affected by changing image intensities in the space domain, which can arise from changes in illumination direction caused by the direction of the sun and shadowing effects. Normalization procedures may overcome some of these problems (Clocksin et al., 2002). In the present study, we applied a masking filter; because the number of photos was limited, we tested the mean brightness of dark regions affected by shadows and applied an intensity mask to disregard all pixels with gray values less than 20% of the b/w scale. Furthermore, if more than 50% of the area of a subregion lay within a masked area, the subregion was disregarded. As a result, we are left only with pixel-offset values outside of the shadow region. The results show that the pixel offsets can be more than 15 pixels in consecutive images; this is significantly higher than the noise level, which was found to be of the order of 1.2 pixels in areas hypothesized to be stable (i.e., on the west and east sides of the valley; see figure 3).

Furthermore, we note again that the sampling in time was irregular (photos were taken only if access and weather permitted), which affects the length of the nonnormalized displacement vectors even if the deformation trend is linear. Therefore, the results have to be considered in relation to the sampling intervals.

3. RESULTS

Direct visual observations of the images reveal only very subtle changes at the dome. Between the first and the last image, the elongate portion of the dome lengthens very slightly downward (figure 3). The pixel-offset calculations show much more detail. The results of the digital image correlation DIC are shown in three formats: the displacement vectors, the displacement contours and the divergence Exx+Eyy, which is a measure of strain and is computed from the displacement vectors.

The displacement vectors (figure 5) obtained from the pixel offsets calculated from the two images taken on 18 and 21 September 2006 reveal downward displacements in the central part of the image (figure 5a). This region of displacement is the location of the actively deforming dome of the Merapi volcano. We can distinguish a zone of displacement high on the dome and another zone covering the lower part of the dome, which we refer to as region (1) and region (2), respectively. These two regions experienced the largest displacements. The displacement regions in image pairs from 21–29 September, 12–13 October and 13–15 October show similar patterns. As observed in the image pairs from 29 September–07 October, 7–12 October, 15–23 October and 23–30 October, the vectors show both downward and upward displacements: The upward displacements, which possibly represent "*doming*," affected only the uppermost part of the dome, whereas the lower part experienced downward displacements. Therefore, the displacement vectors reveal that the motions between the upper and lower parts of the dome, as described by region (1) and region (2), were decoupled. Although parts of region (1) may deform downward and other parts deform upwards, region (2) displays downward displacements in all of the correlated image pairs. These observations provide indications of the forces that cause the deformations, which are discussed further below.

The displacement contours (figure 6) are given in the y-direction only because the vertical direction is most relevant to these deformations. The red colors indicate downward displacements, and the blue colors indicate upward displacements. Regions (1) and (2) can be most clearly distinguished in the image pairs from 18–21 September and 29 September–07 October. Both regions show downward displacements that are separated by a region of very small displacement (or displacement that is not resolved by the camera). Opposite motions in the two regions are also found in the image pairs from 07–12 October, 15–23 October and 23–30 October. The displacement contour plots show that variation of the location of the limiting area of the region (1) is minimal, whilst the length of the region (2) varied downslope.

The divergence (figure 7) is a measure of the two-dimensional strain field that further defines the limits of the regions described above and other features. In the image pair from 18–21 September, for instance, the uppermost region of the dome experienced a positive divergence (volume increase). A second zone of positive divergence is found below the zone, where the valley narrowed and was bounded by two zones of negative divergence (or volume decrease). Other image pairs illustrate features that were similar, although less well expressed, such as on 7–12 October, 12–13 October and 13–15 October.

In summary, the displacement vectors and contours reveal two main zones of deformation. One zone is located within the upper dome (region 1), and the second is located within the southward-flowing part of the dome (region 2). The divergence plots show that these regions are commonly separated by a zone of high strain that is first positive (compressive) and then negative (extensional) and is indicative of a decreasing and increasing velocity profile. The location of this change in strain is associated with the narrow part of the valley. Further implications for the morphology of the valley and its control on the displacement and strain fields are discussed in the following section.

4. DISCUSSION

Lava dome growth and destruction at Mount Merapi has been studied for centuries and has led to a solid understanding of the different phenomena associated with the collapse and generation of hazardous block and ash flows that travel downhill (Voight et al., 2000a and references therein). Because of the threats such pyroclastic flows pose, the failure initiation and deformation processes of domes and their coulées are of interest for many dome-building volcanoes. However, the deformation and strain fields of domes have been directly identified in the field in only very few cases (Major et al., 2009; Poland et al., 2008; Wadge et al., 2008). These rare accounts of dome deformation have relied on camera monitoring and other indirect methods such as radar technologies. More commonly, deformations of the flanks of a dome-building volcano are interpreted indirectly to provide insights on dome-building processes (Carn et al., 2004; Jousset and Okada, 1999; Voight et al., 2000b). Because of the hazards and technical difficulty associated with measuring displacements at an active dome, the understanding of dome deformations relies on numerical and experimental modeling (Fink and Griffiths, 1998; Griffiths and Fink, 1997; Hale et al., 2009a). Our study of the 2006 Merapi dome using photogrammetry and computer-imaging methods is one of the few cases in which dome deformations have been quantified.

Because of the difficulties associated with monitoring the deformation of extruding domes, they are commonly still characterized as idealized near-spherical extrusions in the summit region of the volcano. Only recently three dimensional pictures of lava domes have been elaborated (James and Varley, 2012). The relationship between endogenous and exogenous deformation processes remains poorly constrained. At the Merapi volcano, decades of visual observations have allowed us distinguish between the growing dome and the coulée, which is a particular type of lava flow that is a hybrid of a flow and a dome (Van Bemmelen, 1949). These early accounts distinguished a dome from a coulée using descriptive terms. As our study suggests, the kinematics, deformation and strain of these features differ.

The transition of a dome to a coulée is a transition from endogenous to exogenous growth and is thought to be mainly slope dependent (Van Bemmelen, 1949; Voight et al., 2000a). Lava domes and coulées grow and spread when they exceed a stability threshold that is controlled by the strength, thickness and slope, their failure causing a type of pyroclastic flows called block-and-ash flows (Fink and Anderson, 2000; Francis, 1993). At the Merapi volcano, the different types of gravitational collapses include *Guguran* (the Indonesian term for relatively small lava-block rockfalls) and *Awan Panas* (large, glowing clouds, also referred to as block-and-ash flows). Because pyroclastic flows are linked also with dome talus collapses, subtle deformations of both a dome and its coulée are important in monitoring the volcanic hazard. The approach to studying dome growth that we have presented in this study has several limitations. We used photographs taken from the same position. The quality and temporal resolution of the photos taken from other observatory posts did not allow for the tracking of individual pixels. Because the viewing geometry is a near two-dimensional field of view only, the absolute displacements were not addressed in this paper. Future camera monitoring efforts will have, in addition, to be combined with other independent data, such as from seismic networks, EDM or GPS instrumentation, allowing also to validate or challenge findings such as described in this paper.

We described a rough pixel-to-meter conversion. However, this translation is strongly dependent upon topography and distance and on camera distortion parameters that have not been corrected for. Therefore, we recommend caution when interpreting such results quantitatively, unless they are thoroughly validated.

Despite the limitations described above, our study reveals that the extruding and deforming dome of Merapi, as measured from the photographs from 18 September to 30 October, is not uniform. We distinguished two main regions of displacement:

(1) A region within the upper part of the dome, which is associated with upward-directed pixel offsets during periods of dome growth and with downward-directed vectors during gravity-driven deformation.
(2) A region at the middle and lower parts of the dome, which is identified as the location of a coulée and displays downward displacements in all images.

To further investigate the location and nature of the limits of these two regions, we also computed the strain field, which identified a significant transition from compression to extension across the two regions.

Figure 8a shows a satellite image taken on 11 September 2006, which is only one week before the image sequence described in this paper begins. The eruptions prior to 2006 were directed to the southwest, whereas the 2006 eruption incised the deep Gendol Valley to the south-southeast (Charbonnier and Gertisser, 2009). The Gendol Valley is identified by the darker image intensities in figure 8 and is enclosed by a steep amphitheater, as shown in figure 3. The outline of this amphitheater and the traces of the walls that bound the Gendol Valley are shown by the solid line in figure 8. We interpret the dome as the blocky extrusion that appears near the summit and in the coulée and talus farther south. Furthermore, we identify the narrowest segment of the valley, which is referred to as a “bottleneck” in figure 8.

We projected the combined displacement vectors and divergence field onto the aerial image in figure 8 to better locate the regions of deformation and define the morphological context. We used the prominent morphological features observed in the field and in aerial photographs to manually geocode the two-dimensional field of view as observed from the Deles location. We used six ground-control points (*GCPs*, shown as hexagons in figure 8a). Although such a transformation is geometrically difficult and remains approximate, this illustration contributes to our understanding of emplacement processes and the definition of the two main divergence zones, as illustrated in figure 8b for the image pair from 18–21 September 2006. The upper dome is likely to be associated with near-radial displacements, which are shown in the photos by upward pixel offsets during periods of dome growth and downward offsets during gravity-driven spreading of the dome, with velocities decreasing with distance. Positive strain (expansion) and an acceleration of the coulée are found at the location of the bottleneck. We note that the same bottleneck might also be the location of a change in downslope morphology or steepening.

Accelerations in the growth rate of domes and coulées are typically described in terms of changes of the underlying slope (Platz et al., 2012). Our study reveals that the displacement of the coulée is downhill and is largely unaffected by the conditions of extrusion and endogenous growth in the upper parts of the dome. Therefore, the short-term dynamics of a coulée are not related to the dome extrusion rates. Assuming that the flow of a coulée is comparable to other dynamic flow processes, such as ice or rock glaciers, we speculate that increasing velocities could be related to (a) an increasing accumulation zone, (b) reduced friction inside the flow or at the base, (c) steeper slopes, (d) unbuttressing of the talus region by erosion and collapse and (e) narrowing of the enclosing canyon. The latter phenomenon was described by Nakamura et al. (2007) to explain local accelerations in glaciers. Narrowing might occur three-dimensionally; the combination of horizontal and vertical narrowing might act as a bottleneck, where a flow might increase its velocity (Pattyn and Naruse, 2003). If this concept is applied to the Merapi volcano, our observations that dome and coulée flow convergence lead to local acceleration and high-strain zones appear to be sound. A conceptual model of this “dome in a bottleneck” scenario is presented in figure 9.

We identified the bottleneck of the canyon as the reason for the localization of high strains. As discussed in (Voight et al., 2000a), gravitational collapses of domes and coulées occur when the failure strength of the mass is exceeded. Because the failure of a rock mass is strain-rate dependent (Kwasniewski and Takahashi, 2010), a localized divergence change due to a morphologically induced bottleneck might be a favorable location for failure. At Merapi, this bottleneck is the location where failures are most expected to occur. Indeed, the last figure of our photographic dataset, which was taken on 30 October 2006, reveals the presence of intense fumaroles and a presumably open fracture at or slightly below the location of the bottleneck.

Camera monitoring is a standard tool at many volcanoes because it collects important information about the deformation as well as degassing and other states of activity. However, stable camera positions and optical parameters have only been used in a few cases (Major et al., 2009; Major et al., 2008; Poland et al., 2008). At Merapi, photographs from similar positions have been contributing to our understanding of the volcano for many decades (Voight et al., 2000a) and have been systematically managed since 1993: Photographs of the 1994 dome were taken almost daily (Ratdomopurbo, 1995). After 2006, however, the importance placed on systematic photography had reduced for both research and monitoring. Therefore, in 2010, neither clearly defined absolute deformation data nor other detailed pre-, syn- or after-eruption photographs were available, allowing reconstruction of the large scale deformations.

Another reason for the lack of data is that most of the eruption occurred when the summit was obscured, which made other geophysical and remote-sensing techniques difficult to apply (Surono et al., 2012). This challenge highlights the main weaknesses of any camera-based monitoring program: the need to have a clear view of the volcano and the need for fixed camera positions. Therefore, in a collaboration among the three institutions that coauthored this publication (GFZ, CVGHM and UGM), a new set of time-lapse cameras was recently installed at several fixed positions. Photographs are taken at defined intervals using digital controllers and provide several views of the dome with the hope of capturing the growth of the next dome at high temporal and spatial resolutions and with a stable optical configuration.

5. CONCLUSIONS

Camera records of the Merapi dome from September and October 2006 were used in a detailed pixel offset study allowing the distinguishing of displacement in two regions of the dome. The regions are found to be defined by external morphology. Significant accelerations of the dome and the coulée occurred at a location where the enclosing valley narrows. Convergence of a flowing rock mass into a "bottleneck" is found to be associated with high-strain regions as well as a localized increase in velocity. Therefore, the flux of lava domes and coulées is found to be strongly controlled by the preexisting and evolving morphometry of the substratum and the surrounding valleys, which affect the dome growth and the strain and displacement of a flowing coulée. Because strain localizations were seen to have developed in the same region, we argue that the occurrence and dimensions of rock failure and gravity-driven collapses are affected by the narrow paths in the drainage valley.

6. ACKNOWLEDGEMENTS

We thank our colleagues at BPPTK-CVGHM and UGM for support in the field. The manuscript benefited from thoughtful and constructive reviews by Katharine Bull and Nick Varley, and an anonymous reviewer. We acknowledge financial support from the Helmholtz Fund "Initiating and Networking" and the GFZ Potsdam.

7. REFERENCES

Abdurachman, E.K., Bourdier, J.L. and Voight, B., 2000. Nuees ardentes of 22 November 1994 at Merapi volcano, Java, Indonesia. J. Volcanol. Geotherm. Res., 100(1-4): 345-361.

Adrian, R.J., 1991. Particle-imaging techniques for experimental fluid mechanics. Ann Rev Fluid Mech, 23: 261-304.

Calder, E.S., Luckett, R., Sparks, R.S.J. and Voight, B., 2002. Mechanisms of lava dome instability and generation of rockfalls and pyroclastic flows at Soufrière Hills Volcano. In: T.H. Druitt and B.P. Kokelaar (Editors), The eruption of Soufrière Hills Volcano, Montserrat, from 1995 to 1999. Geological Society of London Memoir, London, pp. 173–190.

Carn, S.A., Watts, R.B., Thompson, G. and Norton, G.E., 2004. Anatomy of a lava dome collapse: The 20 March 2000 event at Soufriere Hills Volcano, Montserrat. J. Volcanol. Geotherm. Res., 131(3-4): 241-264.

Charbonnier, S.J. and Gertisser, R., 2009. Numerical simulations of block-and-ash flows using the Titan2D flow model: examples from the 2006 eruption of Merapi Volcano, Java, Indonesia. Bulletin of Volcanology, 71(8): 953-959.

Clocksin, W.F., Quinta da Fonseca, J., Withers, P.J. and Torr, P.H.S., 2002. Image Processing Issues in Digital Strain Mapping. Proc SPIE, 4790: 384-395.

Fink, J.H. and Anderson, S.W., 2000. Lava domes and Coulees. Academic Press, 307-319 pp.

Fink, J.H. and Griffiths, R.W., 1998. Morphology, eruption rates, and rheology of lava domes: Insights from laboratory models. J Geophys Res-Sol Ea, 103(B1): 527-545.

Francis, P., 1993. Volcanoes, a Planetary Perspective. Clarendon Press, Oxford, 1-443 pp.

Griffiths, R.W. and Fink, J.H., 1997. Solidifying Bingham extrusions: a model for the growth of silicic lava domes. J. Fluid Mech., 347: 13-36.

Hale, A.J., Calder, E.S., Loughlin, S.C., Wadge, G. and Ryan, G.A., 2009a. Modelling the lava dome extruded at Soufriere Hills Volcano, Montserrat, August 2005-May 2006 Part II: Rockfall activity and talus deformation. J. Volcanol. Geotherm. Res., 187(1-2): 69-84.

Hale, A.J., Calder, E.S., Wadge, G., Loughlin, S.C. and Ryan, G.A., 2009b. Modelling the lava dome extruded at Soufriere Hills Volcano, Montserrat, August 2005-May 2006 Part I: Dome shape and internal structure. J. Volcanol. Geotherm. Res., 187(1-2): 53-68.

Hartmann, M.A., 1934. Die Vulkanische Tätigkeit des Merapi Vulkanes (Mittel Java) in seinem östlichen Gipfelgebiete zwischen 1902 und 1908. De Ingenieur in Nederlandsch Indie, IV. Mijnbouw en Geologie, 1(5): 62–73.

Hartmann, M.A., 1935. Die Ausbrüche des G. Merapi (Mittel- Java) bis zum Jahre 1883. Neues Jahrb. für Mineral., 75: 127–162.

James, M.R. and Varley, N., 2012. Identification of structural controls in an active lava dome with high resolution DEMs: Volcán de Colima, Mexico. Geophysical Research Letters, 39(22): 5.

Jousset, P., Dwipa, S., Beauducel, F., Duquesnoy, T. and Diament, M., 2000. Temporal gravity at Merapi during the 1993-1995 crisis: An insight into the dynamical behaviour of volcanoes. J. Volcanol. Geotherm. Res., 100(1-4): 289-320.

Jousset, P. and Okada, H., 1999. Post-eruptive volcanic dome evolution as revealed by deformation and microgravity observations at Usu volcano (Hokkaido, Japan). J. Volcanol. Geotherm. Res., 89(1-4): 255-273.

Kwasniewski, M. and Takahashi, M., 2010. Strain-based failure criteria for rocks: State of the art and recent advances. Rock Mechanics in Civil and Environmental Engineering: 45-56.

Major, J.J., Dzurisin, D., Schilling, S.P. and Poland, M.P., 2009. Monitoring lava-dome growth during the 2004-2008 Mount St. Helens, Washington, eruption using oblique terrestrial photography. Earth and Planetary Science Letters, 286(1-2): 243-254.
Major, J.J., Kingsbury, C.G., Poland, M.P. and LaHusen, R.G., 2008. Extrusion rate of the Mount St. Helens lava dome estimated from terrestrial imagery, November 2004-December 2005. U S Geological Survey Professional Paper, Report: P 1750: 237-255.
Nakamura, K., Wakabayashi, H., Doi, K. and Shibuya, K., 2007. Ice flow estimation of Shirase Glacier by using JERS-1/SAR image correlation. Igarss: 2007 Ieee International Geoscience and Remote Sensing Symposium, Vols 1-12: 4213-4216.
Pan, B., Qian, K., Xie, H. and Asundi, A., 2009. Two-dimensional digital image correlation for in-plane displacement and strain measurement: a review. Meas. Sci. Technol., 20: 062001 (062017pp).
Pattyn, F. and Naruse, R., 2003. The nature of complex ice flow in Shirase Glacier catchment, East Antarctica. J Glaciol, 49(166): 429-436.
Platz, T., Cronin, S.J., Procter, J.N., Neal, V.E. and Foley, S.F., 2012. Non-explosive, dome-forming eruptions at Mt. Taranaki, New Zealand. Geomorphology, 136(1): 15-30.
Poland, M.P., Dzurisin, D., LaHusen, R.G., Major, J.J., Lapcewich, D., Endo, E.T., Gooding, D.J., Schilling, S.P. and Janda, C.G., 2008. Remote camera observations of lava dome growth at Mount St. Helens, Washington, October 2004 to February 2006. U S Geological Survey Professional Paper, Report: P 1750: 225-236.
Ratdomopurbo, A., 1995. Etude sismologique du volcan Mérapi et formation du dôme de 1994, University of Joseph Fourier, Grenoble, 208 pp.
Ratdomopurbo, A. and Poupinet, G., 2000. An overview of the seismicity of Merapi volcano (Java, Indonesia), 1983-1994. J. Volcanol. Geotherm. Res., 100(1-4): 193-214.
Surono, Jousset, P., Pallister, J., Boichu, M., Buongiorno, M.F., Budisantoso, A., Costa, F., Andreastuti, S., Prata, F., Schneider, D., Clarisse, L., Humaida, H., Sumarti, S., Bignami, C., Griswold, J., Carn, S., Oppenheimer, C. and Lavigne, F., 2012. The 2010 explosive eruption of Java's Merapi volcano – a '100-year' event. J. Volcanol. Geotherm. Res., in press: doi: 10.1016/j.jvolgeores.2012.1006.1018.
Van Bemmelen, R.W., 1949. The Geology of Indonesia. Martinus Nijhoff, The Hague, 732 pp.
Voight, B., Constantine, E.K., Siswowidjoyo, S. and Torley, R., 2000a. Historical eruptions of Merapi Volcano, Central Java, Indonesia, 1768-1998. J. Volcanol. Geotherm. Res., 100(1-4): 69-138.
Voight, B. and Elsworth, D., 2000. Instability and collapse of hazardous gas-pressurized lava domes. Geophysical Research Letters, 27(1): 1-4.
Voight, B., Young, K.D., Hidayat, D., Subandrio, Purbawinata, M.A., Ratdomopurbo, A., Suharna, Panut, Sayudi, D.S., LaHusen, R., Marso, J., Murray, T.L., Dejean, M., Iguchi, M. and Ishihara, K., 2000b. Deformation and seismic precursors to dome-collapse and fountain-collapse nuees ardentes at Merapi Volcano, Java, Indonesia, 1994-1998. J. Volcanol. Geotherm. Res., 100(1-4): 261-287.
Wadge, G., Macfarlane, D.G., Odbert, H.M., James, M.R., Hole, J.K., Ryan, G., Bass, V., De Angelis, S., Pinkerton, H., Robertson, D.A. and Loughlin, S.C., 2008. Lava dome growth and mass wasting measured by a time series of ground-based radar and seismicity observations. J Geophys Res-Sol Ea, 113(B8).
Walter, T.R., Wang, R., Zimmer, M., Grosser, H., Luhr, B. and Ratdomopurbo, A., 2007. Volcanic activity influenced by tectonic earthquakes: Static and dynamic stress triggering at Mt. Merapi. Geophysical Research Letters, 34(5).
Watts, R.B., Herd, R.A., Sparks, R.S.J. and Young, S.R., 2002. Growth patterns and emplacement of the andesitic lava dome at Soufrière Hills, Montserrat. Geological Society of London Memoir 21: 115–152.

Young, K.D., Voight, B., Subandriyo, Sajiman, Miswanto and Casadevall, T.J., 2000. Ground deformation at Merapi Volcano, Java, Indonesia: Distance changes, June 1988-October 1995. J. Volcanol. Geotherm. Res., 100(1-4): 233-259.
Zavada, P., Kratinova, Z., Kusbach, V. and Schulmann, K., 2009. Internal fabric development in complex lava domes. Tectonophysics, 466(1-2): 101-113.

FIGURE CAPTIONS

Figure 1: Location of the Merapi volcano on Java, Indonesia (insert), and shaded-relief image of the area of the volcano near the town of Yogyakarta (the city centre is marked by a white square). The camera was located approximately 4 km southeast of the Merapi summit at Deles. The observatories described in the text are shown by symbols. The detailed view of the summit region shown in figure 2 is indicated.

Figure 2: DigitalGlobe satellite image acquired on 11 September 2006, a few days before the commencement of the time lapse photography dataset. The dark region to the southwest (related to the early 2006 eruptive period) and the dark region to the south-southeast (site of the 2006 eruption and collapse climax) are clearly observed. Dome growth was visible in September and October 2006 and was recorded by digital SLR cameras from the south-southeast (Deles, see figure 1).

Figure 3: (a) Detail of a photograph with the growing dome and its flow to the south-southeast. The dome is approximately 120 m in diameter, and the downslope length of the coulée approximately 300 m. All photos were taken in the early morning hours, and the sunlight is from the east (the right side of the photograph). Note shadow effects within the Gendol Valley. (b) Preprocessed time-lapse dataset before applying the pixel-offset calculations. The image intervals are between 1 and 8 days; the lack of visibility of the dome from a distance of 4 km prevented other recordings.

Figure 4: Simplified schematic illustration of the image correlation and pixel-offset computation method. Two images with x and y coordinates were selected and subdivided into n x m pixel subwindows. The reduced size of the subwindows in later passes is not shown here. The intensity function was solved for each subwindow. The distance between a subregion in image 1 and a correlated subregion in image 2 was translated to a pixel-offset value given by a displacement vector. Strain components such as divergence were computed through post-processing.

Figure 5: Results showing displacement vectors. A reference vector is given in (a). Two regions of pixel offsets can be distinguished; region (1) experiences downslope and sometimes upslope (doming) displacements, whereas region (2) shows downslope motion in all image pairs. The two regions appear to behave independently.

Figure 6: Results showing contours of y-displacements. The color code is given in (a), and the unit is pixels. The two regions of displacement are observed during episodes of spreading and during episodes of doming within region 1.

Figure 7: Results showing the divergence, which is based on the strain tensors. The color code is given in (a). The regions of displacement (cf. figure 6) are delimited by

changes in divergence from positive to negative. The divergences show compression (green) where region 1 and 2 are decelerating and expansion (red) at locations where region 2 is accelerating. This systematic pattern of divergence changes is most clearly expressed in panels a, b, c, d and g and is more complex in panels e, f and h. The high-strain zones are presumed to be the transition zones from the dome to the coulée.

Figure 8: Morphometric interpretation of the strain and displacement results. (a) Satellite image (same as in figure 2) with morphologic interpretation of the dome, coulée and the limiting amphitheater (solid black line). Hexagons indicate ground-control points used to overlie the displacement and divergence map. (b) Displacement and divergence map showing close relationship of the two main displacement regions and localization of the high-strain zone near the bottleneck.

Figure 9: Conceptual model of "a dome in a bottleneck", (a) real geometry at Merapi volcano, (b) idealized geometry. The accumulation zone in upper region experiences fast displacement (shown by reddish color). Thereafter, the velocity of the lava flow (coulée) is controlled mainly by the morphometry of the enclosing and underlying edifice, decreasing (yellow color) and increasing again (reddish color). Similar as in a bottleneck, reduction of the dimension of a pipe increases the flow velocity (vel=2) of the coulée.

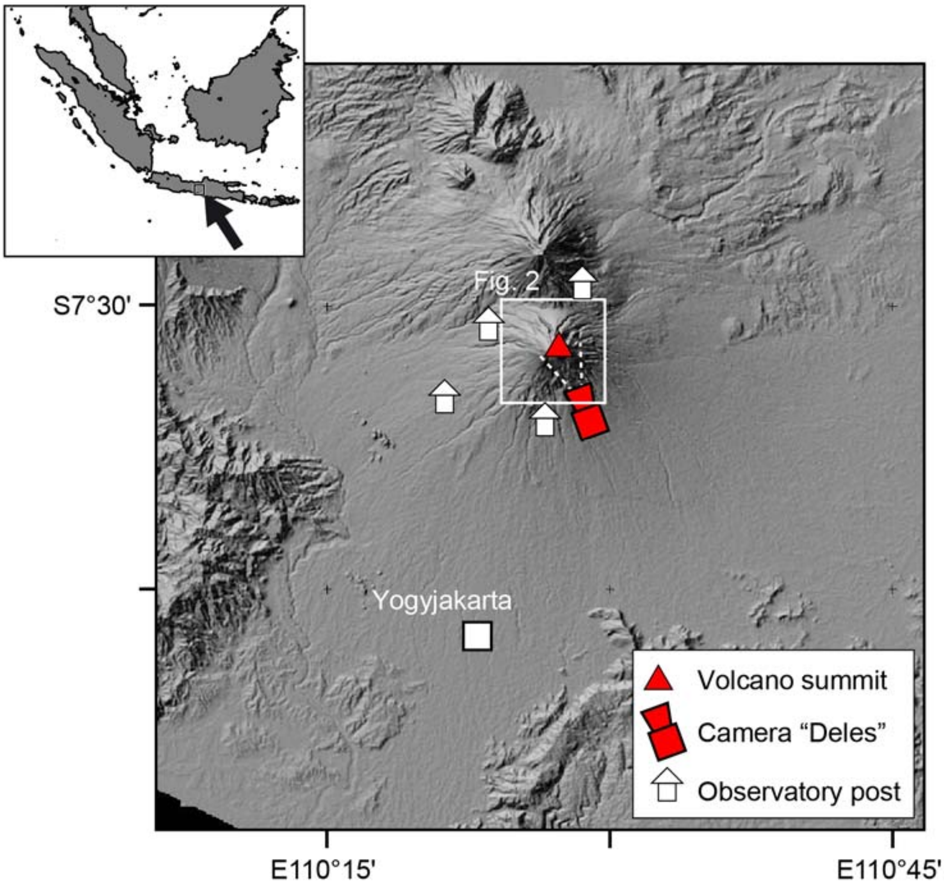
Fig. 2
S7°30'
Yogyjakarta
Volcano summit
Camera “Deles”
Observatory post
E110°15'
E110°45'

Figure 1

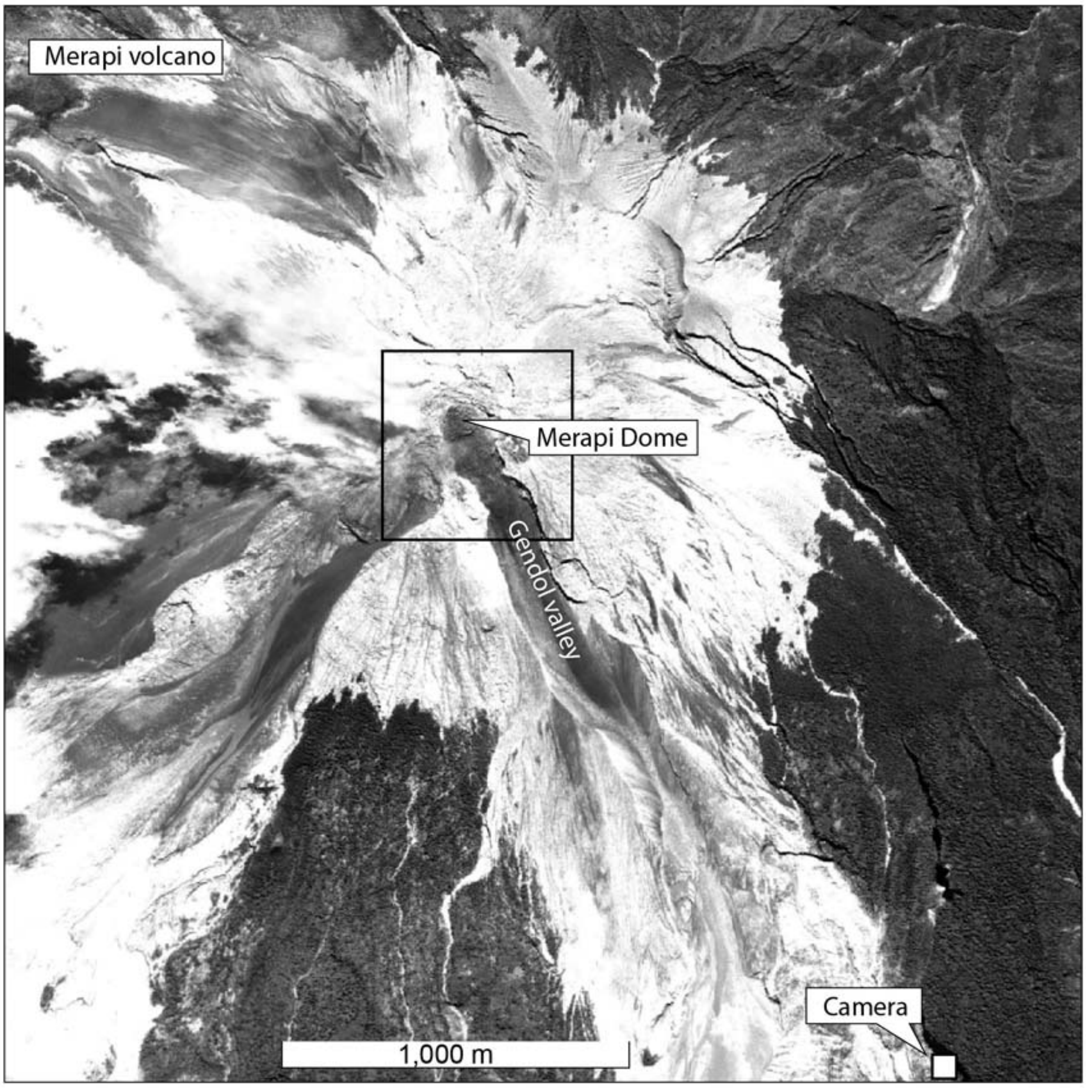

Figure 2

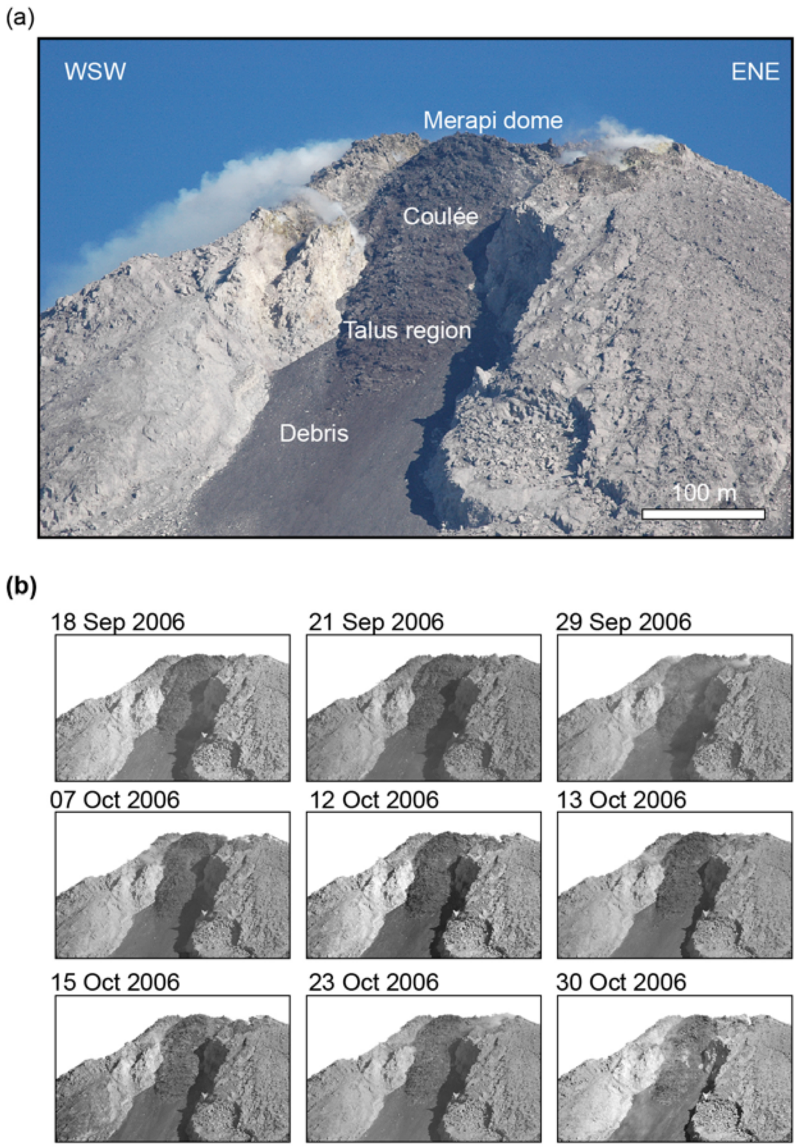
(a)
WSW
ENE
Merapi dome
Coulée
Talus region
Debris
100 m
(b)
18 Sep 2006
21 Sep 2006
29 Sep 2006
07 Oct 2006
12 Oct 2006
13 Oct 2006
15 Oct 2006
23 Oct 2006
30 Oct 2006

Figure 3

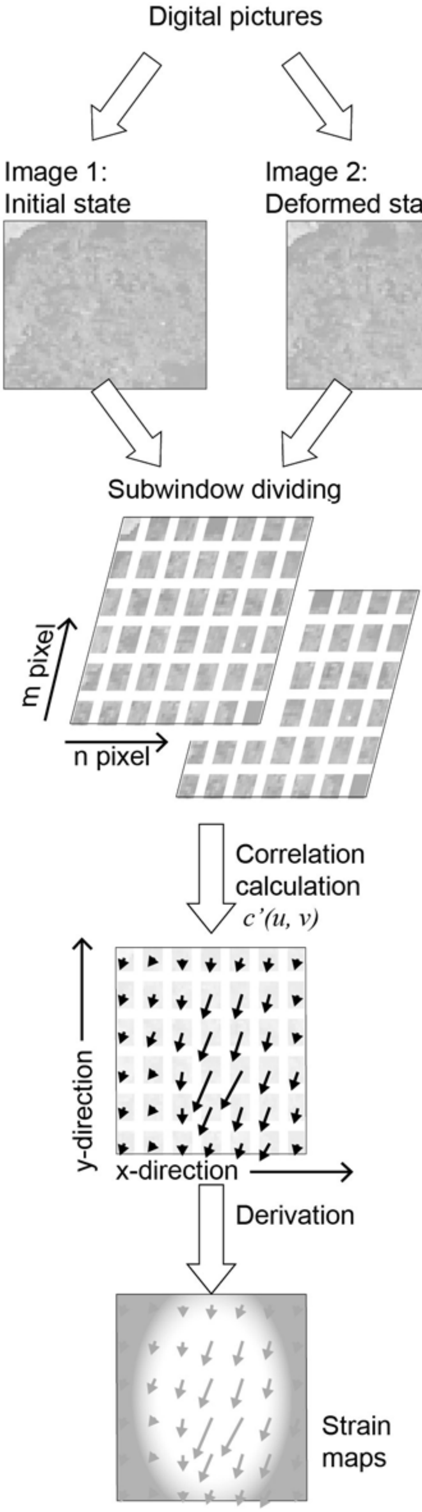
Digital pictures
Image 1:
Initial state
Image 2:
Deformed state
Subwindow dividing
m pixel
n pixel
Correlation
calculation
c'(u, v)
y-direction
x-direction
Derivation
Strain
maps

Figure 4

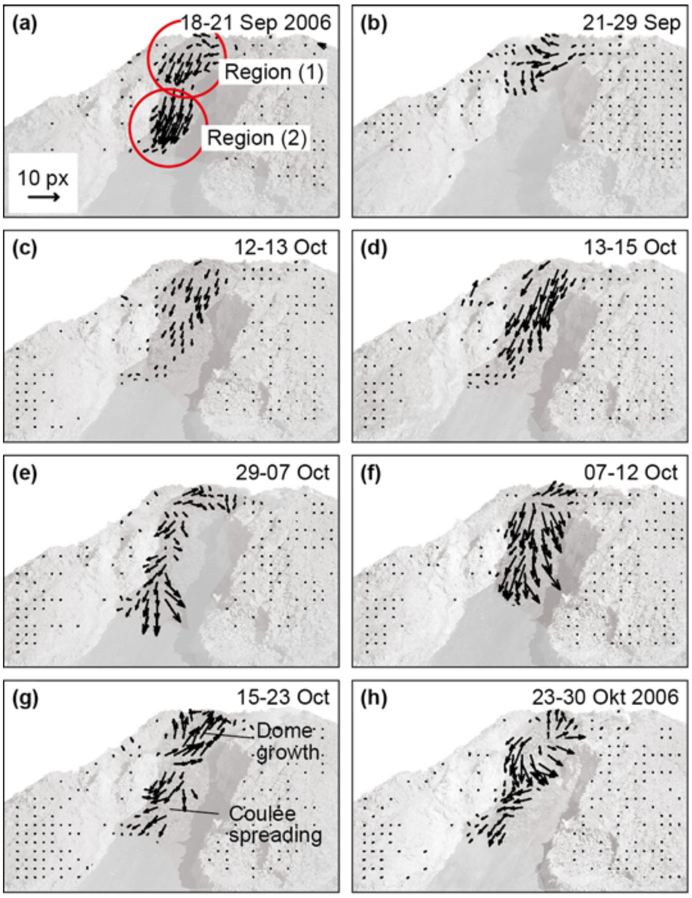
(a)
18-21 Sep 2006
Region (1)
Region (2)
10 px
(b)
21-29 Sep
(c)
12-13 Oct
(d)
13-15 Oct
(e)
29-07 Oct
(f)
07-12 Oct
(g)
15-23 Oct
Dome growth
Coulée spreading
(h)
23-30 Okt 2006

Figure 5

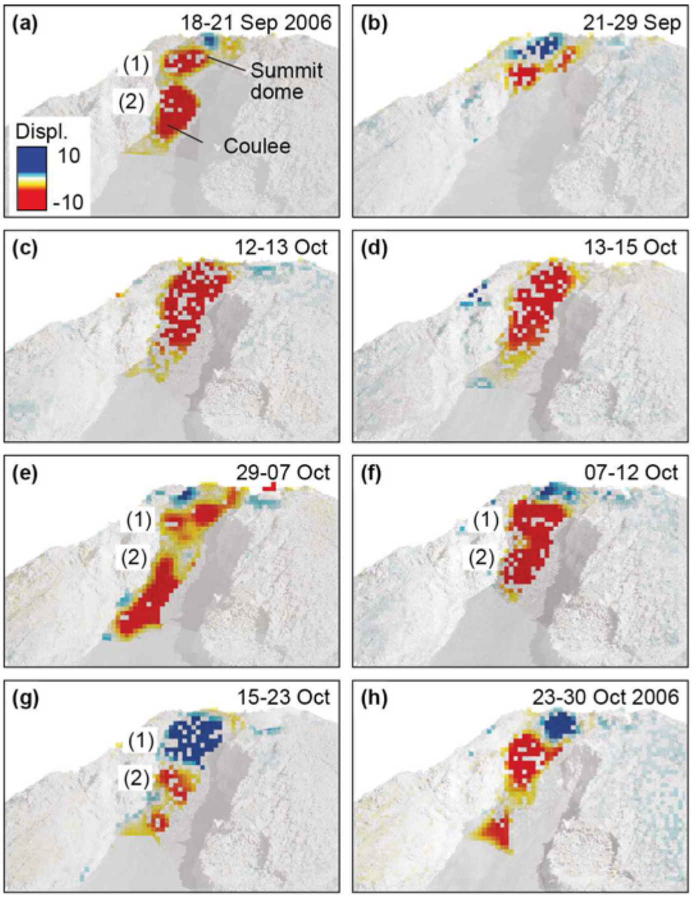
(a)
18-21 Sep 2006
(1)
(2)
Summit dome
Coulee
Displ.
10
-10
(b)
21-29 Sep
(c)
12-13 Oct
(d)
13-15 Oct
(e)
29-07 Oct
(1)
(2)
(f)
07-12 Oct
(1)
(2)
(g)
15-23 Oct
(1)
(2)
(h)
23-30 Oct 2006

Figure 6

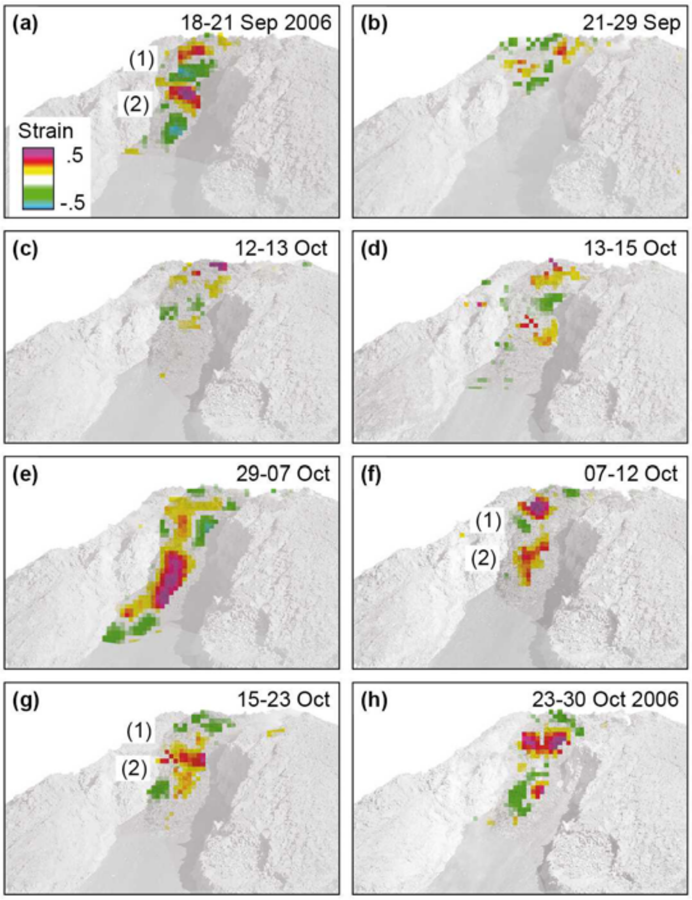
(a)
18-21 Sep 2006
(1)
(2)
Strain
.5
-.5
(b)
21-29 Sep
(c)
12-13 Oct
(d)
13-15 Oct
(e)
29-07 Oct
(f)
07-12 Oct
(1)
(2)
(g)
15-23 Oct
(1)
(2)
(h)
23-30 Oct 2006

Figure 7

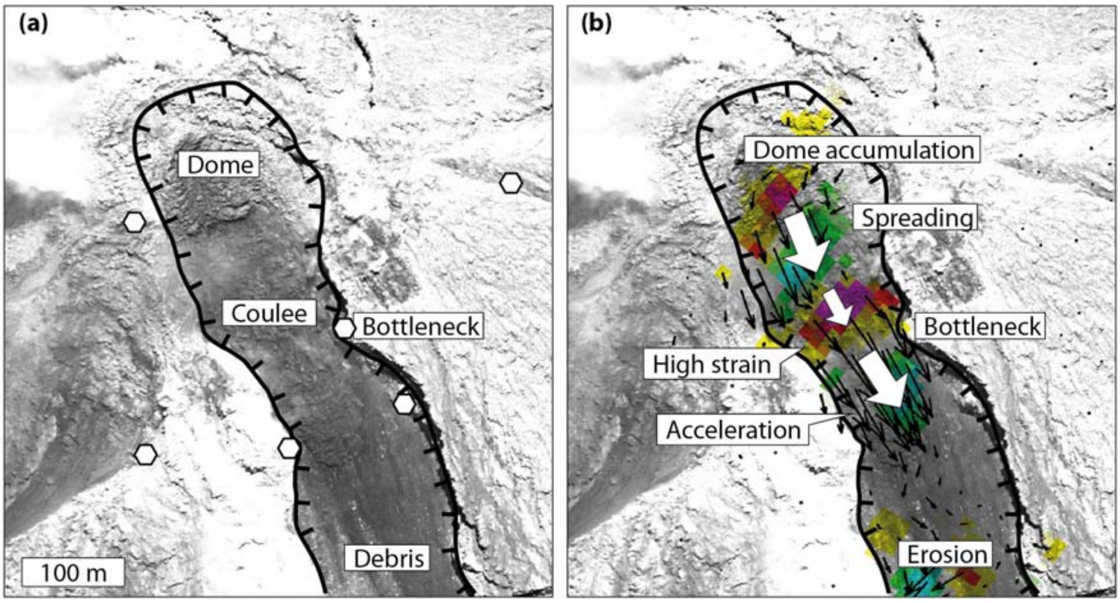
(a)
Dome
Coulee
Bottleneck
Debris
100 m
(b)
Dome accumulation
Spreading
Bottleneck
High strain
Acceleration
Erosion

Figure 8

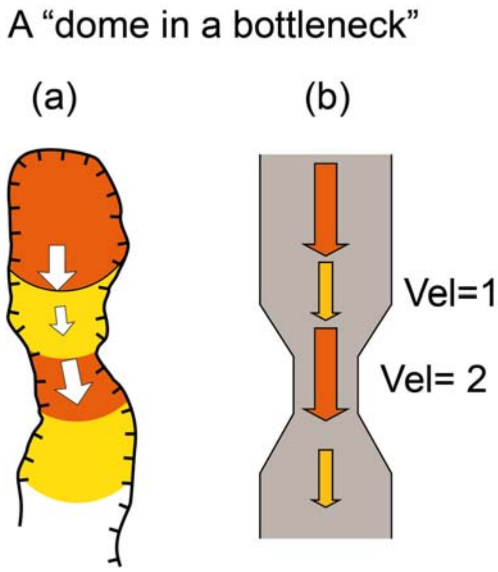

Figure 9